Steel and Composite Structures, *Vol. 30, No. 2* (*2019*) *123-140*
DOI: https://doi.org/10.12989/scs.2019.30.2.123

Rotational capacity of H-shaped steel beams under cyclic pure bending

Liang-Jiu Jia [1a], Yafeng Tian [2b], Xianzhong Zhao [*3] and Siyuan Tian [3c]

[1] *Department of Disaster Mitigation for Structures, Tongji University, Shanghai, 200092, China*
[2] *Key Laboratory of Civil Engineering Structure and Mechanics, Inner Mongolia University of Technology, Hohhot 010051, China*
[3] *Deparment of Structural Engineering, Tongji University, Shanghai, 200092, China*

(*Received April 15, 2018, Revised January 7, 2019, Accepted January 20, 2019*)

Abstract. This paper presents experimental study on effects of width-to-thickness ratio and loading history on cyclic rotational capacity of H-shaped steel beams subjected to pure bending. Eight Class 3 and 4 H-shaped beams with large width-to-thickness ratios were tested under four different loading histories. The coupling effect of local buckling and cracking on cyclic rotational capacity of the specimens was investigated. It was found that loss of the load-carrying capacity was mainly induced by local buckling, and ductile cracking was a secondary factor. The width-to-thickness ratio plays a dominant effect on the cyclic rotational capacity, and the loading history also plays an important role. The cyclic rotational capacity can decrease significantly due to premature elasto-plastic local buckling induced by a number of preceding plastic reversals with relative small strain amplitudes. This result is mainly correlated with the decreasing tangent modulus of the structural steel under cyclic plastic loading. In addition, a theoretical approach to evaluate the cyclic rotational capacity of H-shaped beams with different width-to-thickness ratios was also proposed, which compares well with the experimental results.

Keywords: cyclic rotational capacity; local buckling; ductile fracture; pure bending; H-shaped beam; steel

1. Introduction

In the past decades, H-shaped steel beams have been playing essential roles in many kinds of structures and a number of studies on seismic performance of H-shaped steel beams have been conducted. Rotational capacity of H-shaped beams under combined compression and bending had been investigated in the literature (Nakashima 1994, Gioncu and Petcu 1997a, b, Hasegawa and Ikarashi 2014). Gioncu *et al*. (2012) and Anastasiadis *et al*. (2012) proposed a prediction method for the rotational capacity of H-shaped beams under cyclic loading. Cheng *et al*. (2013) experimentally studied the load-carrying capacity and hysteretic properties of H-shaped steel beam-columns with large width-to-thickness ratios under cyclic bending about the weak axis. Akrami and Erfani (2015) investigated the effect of local web buckling on the cyclic behavior of reduced web beam sections. Elkady and Lignos (2015); Newell and Uang (2008); Lee and Lee (1994) investigated ductility and strength of H-shaped beams under cyclic loading histories. In addition, there are a number of studies on local buckling strength and ductility of steel beams with perforations in the web (e.g., Kwon *et al*. 2014, Erdal 2015, Morkhade and Gupta 2017).

Besides, the effect of local buckling on rotational capacity of steel shear link beams was studied by some researchers (Kasai and Popov 1986a, b, Richards and Uang 2005), in which failures of the beams were mainly due to local buckling of the beam webs. However, seismic performance of H-shaped beams under cyclic pure bending has seldom been investigated, and studies on coupling effects of local buckling and subsequent cracking of structural members are more limited (Jia *et al*. 2014). There are a number of studies on ultra-low-cycle fatigue (ULCF) behaviors of steel components, e.g., Ge *et al*. 2014, Jia *et al*. 2016, Chen *et al*. 2017, Zhao *et al*. 2018. A number of studies on ULCF behaviors of metallic dampers are also conducted, e.g., Jia *et al*. 2017, 2018a, b, 2019. Class 3 and 4 steel members are widely employed in gabled frames and increasingly employed in low-rise prefabricated steel structures for their high structural efficiency. Most of these structures are in regions with high seismic risks. Their seismic performance is of great importance. However, research on seismic behaviors of Class 3 and Class 4 H-shaped steel members under cyclic pure bending are limited. These steel members with large width-to-thickness ratios are more apt to fail due to coupled effects of buckling and cracking under ULCF loading.

This study aims to investigate seismic performance of H-shaped steel beams under different ULCF loading histories, especially for beams with Class 3 and 4 cross sections. In this paper, the impacts of the loading history on failure modes, strength, cyclic rotational capacity and cumulative energy dissipation capacity were investigated using eight specimens under four different ULCF loading histories. The experimental results were employed to establish a prediction formula of the ULCF life of Class 3 and 4 beams using the Manson-Coffin rule (Manson 1953, Coffin 1954). In addition, finite element models were established to investigate the local stress and strain states

---

[*] Corresponding author, Professor,
E-mail: x.zhao@tongji.edu.cn
[a] Associate Professor, E-mail: lj_jia@tongji.edu.cn
[b] Assistant Professor, E-mail: tyf@imut.edu.cn
[c] Graduate Student

http://www.techno-press.org/?journal=scs&subpage=6 ISSN: 1229-9367 (Print), 1598-6233 (Online)

during the pre- and post-local-buckling stages for Class 3 and 4 H-shaped steel beams. Finally, a theoretic model was developed to evaluate the relationship between the cyclic rotational capacity and the width-to-thickness ratio of the H-shaped beams under ULCF loading histories. The coefficient in the proposed formula was obtained based on experimental results of nine specimens with three different width-to-thickness ratios, i.e., Class 1 to 3 cross sections, where elasto-plastic buckling occurred. The formula had a simple expression, in which only the effect of the width-to-thickness ratio was included. Comparison between the experimental and the theoretical results indicates acceptable accuracy of the newly proposed formula.

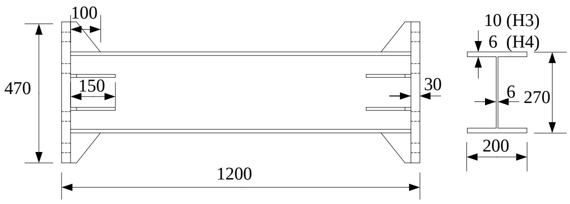

Fig. 1 Cross section of specimens

2. Experimental program

2.1 Design of specimens

Eight H-shaped steel beams made of Chinese low alloy structural steel Q345B, with a nominal yield strength of 345 N/mm^2 were designed and manufactured in this study, with four specimens each for Class 3 and Class 4 specimens. The Class 3 specimens had the same cross section of 270 mm × 200 mm × 6 mm × 10 mm (height × width × web thickness × flange thickness), and the Class 4 ones 270 mm × 200 mm × 6 mm × 6 mm as shown in Fig. 1. The length of all the specimens was 1200 mm, and the length-to-width ratio is around 4.4, which is considered to be short enough to avoid global buckling and long enough to avoid the boundary effect. The flanges and webs are both categorized into four classes according to the width-to-thickness ratios in EC3 (CEN 2005) and the threshold values are given in Table 1. In this study, the beam flanges of the specimens

Table 1 Cross sectional parameters

Specimens	$h \times b \times t_w \times t_f$	$c_w/t_w \le X_w$	Web class	$c_f/t_f \le X_f$	Flange class
H3	270×200×6×10	$41.7 \le 59.4$	1	$8.3 < 9.7 \le 11.6$	3
H4	270×200×6×6	$43.0 \le 59.4$	1	$16.2 > 11.6$	4

*Notes: h, beam height; b, beam width; c_f, net half width of beam flange; c_w, net height of beam web; t_f, thickness of beam flange; t_w, thickness of beam web; X_f, critical width to thickness ratio for flange; X_w, critical width-to-thickness ratio for web (CEN 2005)

Table 2 Measured mechanical properties of steel

Nominal thickness (mm)	Actual thickness (mm)	Yield strength (MPa)	Tensile strength (MPa)	Strain at peak load	Elongation (%)
10	9.93	448	662	0.132	23.4
6	5.7	428	594	0.179	25.2

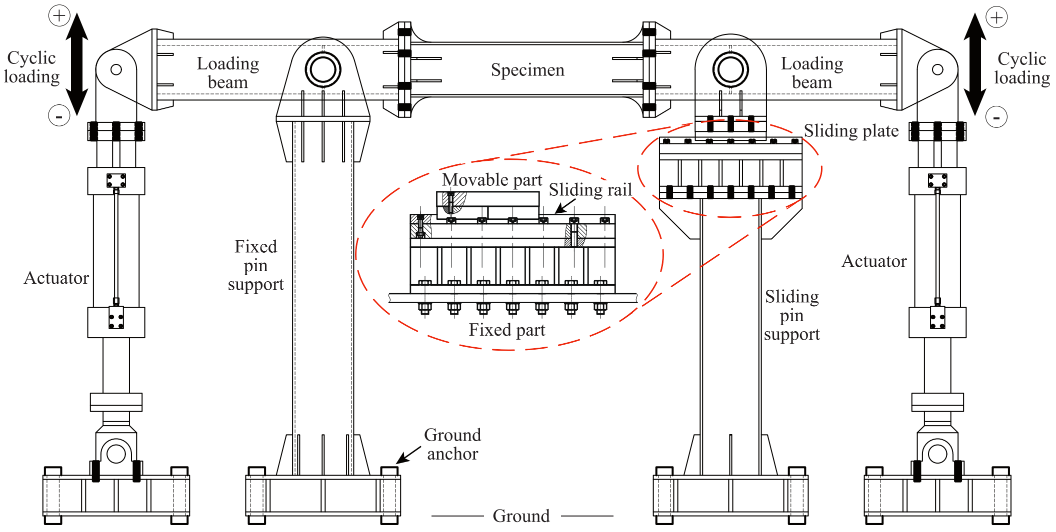

Fig. 2 Test setup (Zhao *et al*. 2018)

most of steel structures.

All the specimens were manufactured by assembling steel plates with different thickness using butt welding. Coupon tests of the steel plates with different thickness were conducted and the measured average mechanical properties are given in Table 2. To connect the H-shaped beams with the loading devices illustrated in Fig. 2, two end plates with a thickness of 30 mm were welded to the two beam ends. Four stiffeners each respectively at the beam-web-to-end-plate joints and the beam-flange-to-end-plate joints were employed to avoid premature failure at the beam ends. It should be noted that the stiffeners at the web were longer than those at the flanges, to avoid the aforementioned failure under cyclic pure bending.

2.2 Test setup

To apply the cyclic pure bending loads to the specimens, a testing device with two loading beams, two supporting columns and two actuators each with a load capacity of ±2000 kN was designed and manufactured as illustrated in Fig. 2. One end of the actuator was pin-connected to the free end of the loading beam, and the other was pin-connected to the bearings made of stiff steel blocks. The bearings were fixed to the laboratory basement using anchor bolts. The two loading beams with the same rectangular cross section were designed, which are strong enough to transfer the loads from the actuators to the specimens. The top ends of the two supporting columns were pin-connected to the loading beams, where the in-plane rotational freedom was released and the rotational freedom along the length of the specimen was restrained. The bottom ends of the supporting columns were rigidly connected to the basement of the laboratory using anchor bolts. A sliding connection between the left loading beam and the supporting column was also designed to release the axial restraining to the specimen at the large deformation stage. The load and displacement capacities of the sliding connection are respectively ±600 kN and ±175 mm, which are large enough for the experimental study in this paper. Quasi-static experiments were conducted and the loading directions were also indicated in Fig. 2, and all the experiments were conducted at room temperature.

2.3 Loading history

Since seismic response of structures under earthquake loading is random, a variety of loading histories considering the loading sequence and amplitude were investigated and four different loading histories were designed. The four loading histories are termed as single full cycle loading, incremental-amplitude loading, de-incremental loading and 2-stage incremental loading as illustrated in Fig. 3.

All the specimens are listed in Table 3, and the numbering of the specimens complies with the following rules, which can be illustrated by Specimen H3-S. “H3” denotes Class 3 H-shaped steel beams, and “H4” Class 4 ones. “S” denotes the single full cycle loading history, and “I”, “D” and “2” respectively denotes the incremental loading, de-incremental loading and the 2-stage incremental loading histories.

The experiments were all controlled by the net rotation of the specimen, θ, which can be calculated by the displacement and load of the actuator using the following equation as illustrated in Fig. 4

$$\theta = \alpha - \alpha_M = \theta_{Cal} - \alpha_F - \alpha_M \tag{1}$$

where α is the rigid rotation of the loading beam, α_M is the elastic rotation of the loading beam, θ_{cal} is the measured rotation at the loading beam end connecting with the actuator, α_F is the rotation of the loading beam end corres-

Table 3 Experimental results

Specimens	$M_{u,exp}$ (kN.m)	μ_c	$\mu_{\max}$	$M_{b,exp} / M_y$	M_c / M_y	Buckling point	Crack initiation point	Crack initiation location	Rupture location
H3-S	271.3	2.2	3.2	1.00	0.90	0.04rad	0.24rad	Weld toe	Weld toe
H3-I	295.8	12.8	3.7	0.98	1.06	0.03rad (1st cycle)	0.06rad (1st cycle)	Flange	Weld toe
H3-D	294.2	5.5	4.5	1.00	0.98	0.04rad (D-1st cycle)	0.05rad (I-1st cycle)	Flange	Weld toe
H3-2	283.8	20.5	2.7	0.81	1.00	0.02rad (1-12th cycle)	0.04rad (2nd stage-1st cycle)	Weld toe	Weld toe
H4-S	163.0	1.9	2.9	1.00	0.82	0.01rad	0.23rad	Weld toe	Weld toe
H4-I	162.5	5.4	2.6	0.62	0.56	0.01rad (2nd cycle)	0.05rad (1st cycle)	Flange	Flange
H4-D	139.7	6.1	4.7	1.00	0.42	0.01rad (D-1st cycle)	0.04rad (1st cycle)	Weld toe	Flange
H4-2	157.9	5.5	2.0	0.98	0.62	0.01rad (1st stage-1st cycle)	0.03rad (2nd stage-1st cycle)	Weld toe	Weld toe

*Notes: $M_{u,exp}$ = ultimate moment of the experiments; μ_c = cumulative ductility; $\mu_{\max}$ = maximum ductility; $M_{b,exp}$ = experimental maximum moment capacity within the half cycle when buckling occurs; M_c = maximum moment capacity within the half cycle when the first crack initiates; M_y = cross-sectional edge yielding moment. Crack initiation location indicates the location where the first crack initiates and rupture location is the one where the crack first runs through the steel plate thickness

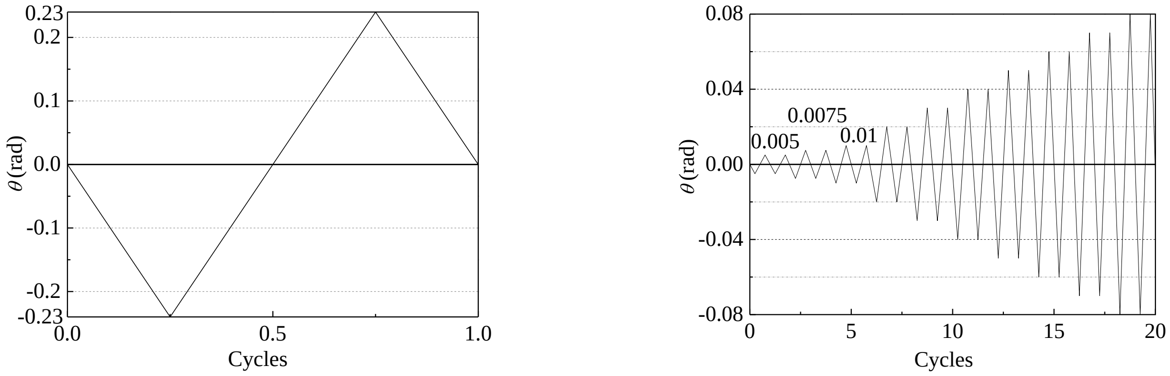

(a) Single full cycle (H1-S)

(b) Incremental (H1-I)

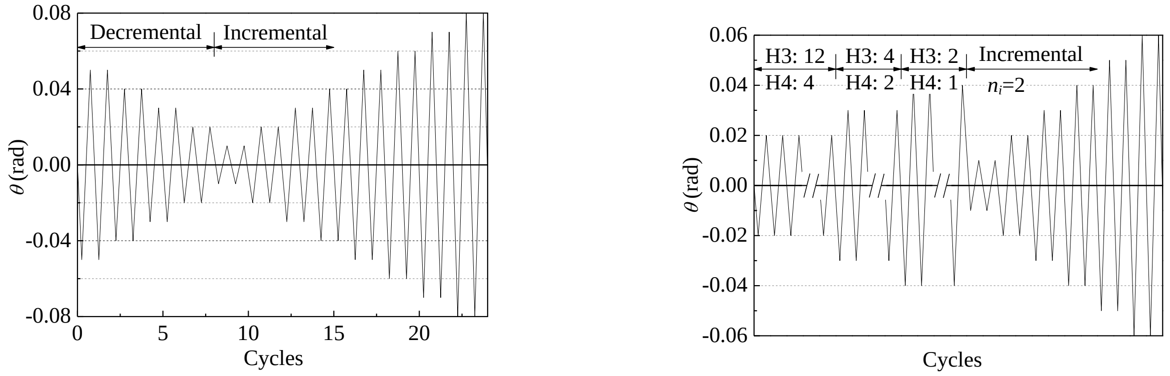

(c) De-incremental (H1-D)

(d) 2-stage incremental (H1-2)

Fig. 3 Loading histories

ponding to elastic deformation of the cantilevered portion of the loading beam under the applied load of the actuator, *F*, shown in Fig. 4.

Under near-field earthquakes such as the 1995 Kobe earthquake and the 1999 Chi-Chi earthquake, structures are subject to pulse-type seismic excitations, the single full cycle loading history shown in Fig. 3(a) was designed to simulate this type of seismic events, which is close to the case of monotonic loading. Considering the rotational capacity of the loading device, the specimens under the single full cycle loading were firstly bended to the full rotational capacity of the loading device, and then a reversal loading was applied.

The cyclic incremental loading history is a widely used loading pattern and a number of loading protocols have been specified in guidelines of many countries, e.g., the ATC-24 loading history (Krawinkler 1992). In this study, the incremental loading history illustrated in Fig. 3(b) is similar to that of ATC-24, where each amplitude was repeated twice to study deterioration of the load-carrying capacity at the corresponding amplitude. Only two elastic amplitude levels were considered in the incremental loading history for the fact that the elastic loading has a minor effect on seismic performance of the steel members where no significant stress concentration within the beams. This is different from those for welded steel beam-to-column connections, where severe stress concentration can occur at the connections, e.g., the weld access hole. The elastic limit is approximately 0.01 rad for the specimens in this study in terms of the beam end rotation angle, θ. For the amplitude within the plastic loading range, the amplitude increment was designed as 0.01.

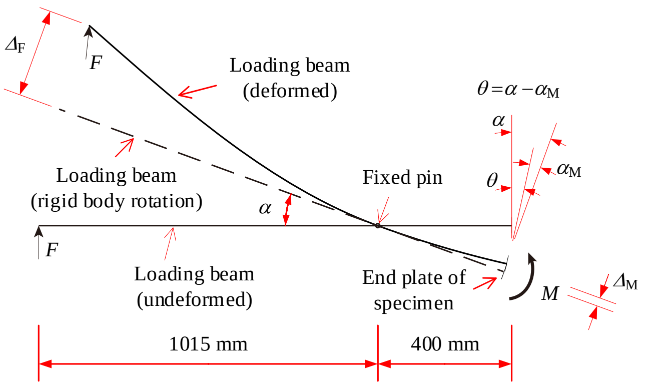

Fig. 4 Calculation of beam end rotation (Zhao *et al*. 2018)

The third loading history shown in Fig. 3(c) consists of two parts, i.e., a decremental amplitude part and an incremental one, which is thus termed as de-incremental loading history in this study. The initial loading amplitude is defined as 0.05 rad considering the fact that the maximum story drift angle under a strong earthquake is also around this value (Krawinkler 1992).

The final loading history shown in Fig. 3(d) is termed as the 2-stage loading history, where the two elastic amplitudes in the incremental loading history are replaced by three constant-amplitude levels exceeding the elastic limit, i.e., 0.02 rad, 0.03 rad and 0.04 rad. For each

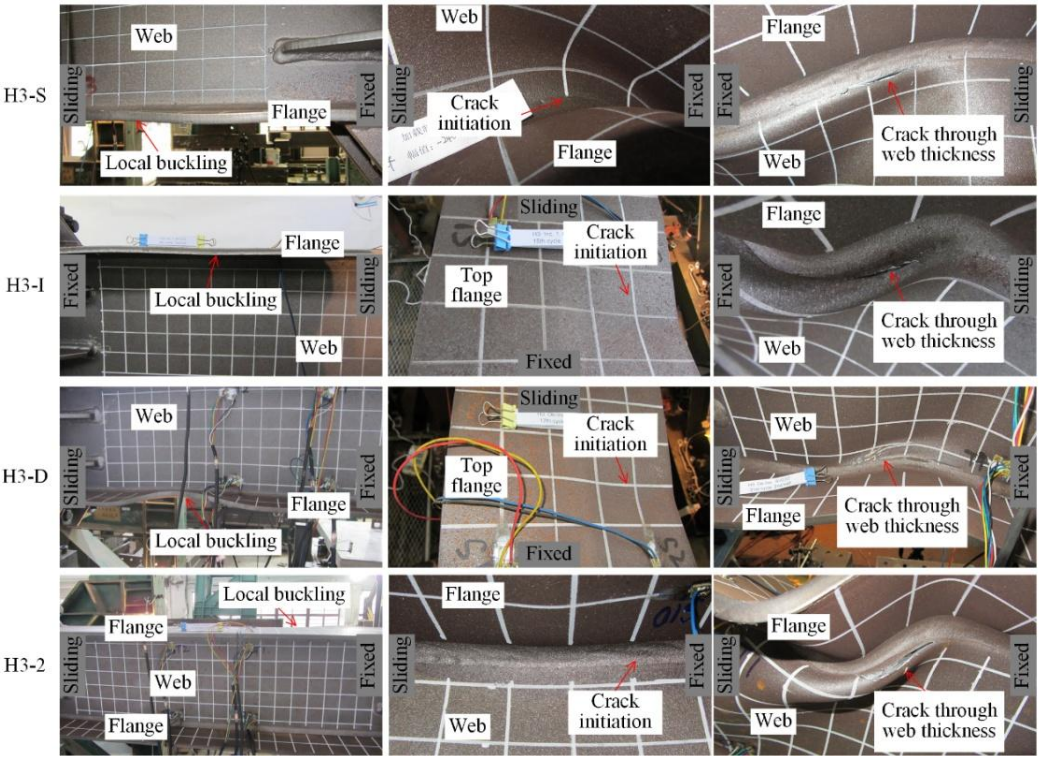

(a) Class 3

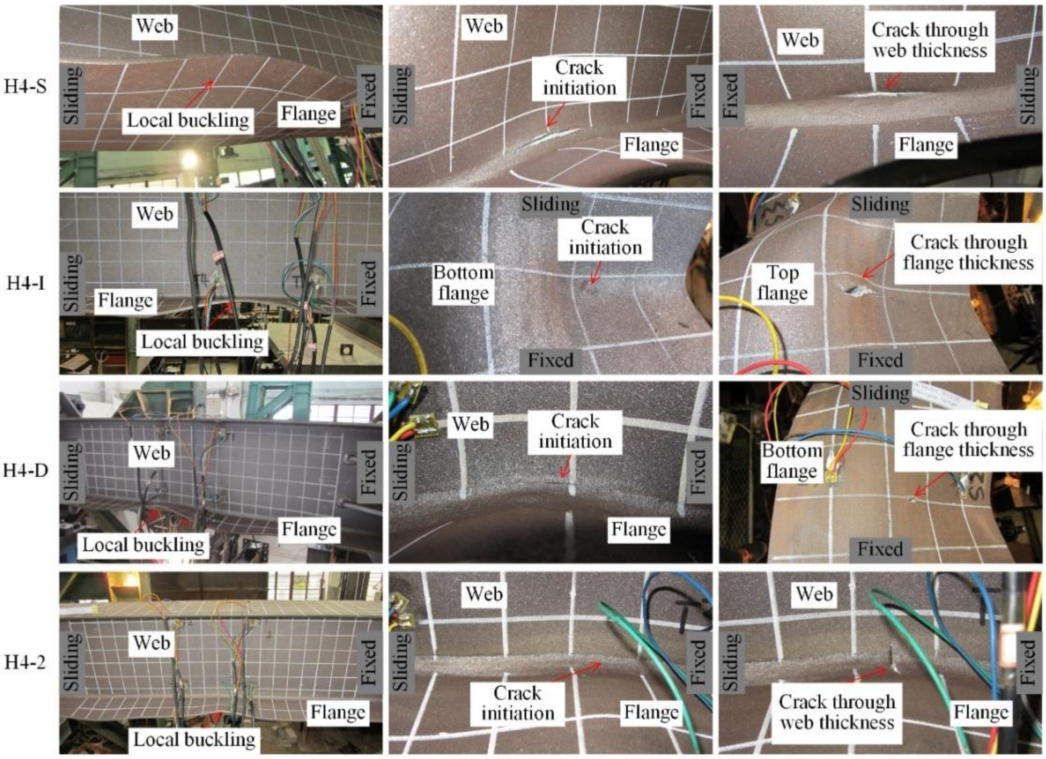

(b) Class 4

Fig. 5 Failure processes of specimens

amplitude level within the first stage, the number of loading cycles was determined when the absorbed plastic energy under that loading amplitude equals to the one under the aforementioned incremental loading history till the peak load. The numbers of loading reversals at the first stage for Class 3 and 4 specimens are also given in Fig. 3(d). For Class 3 specimens, the numbers of loading reversals at the 0.02 rad, 0.03 rad and 0.04 rad amplitude levels are respectively 12, 4 and 2, while these numbers are respectively 4, 2 and 1 for Class 4 specimens.

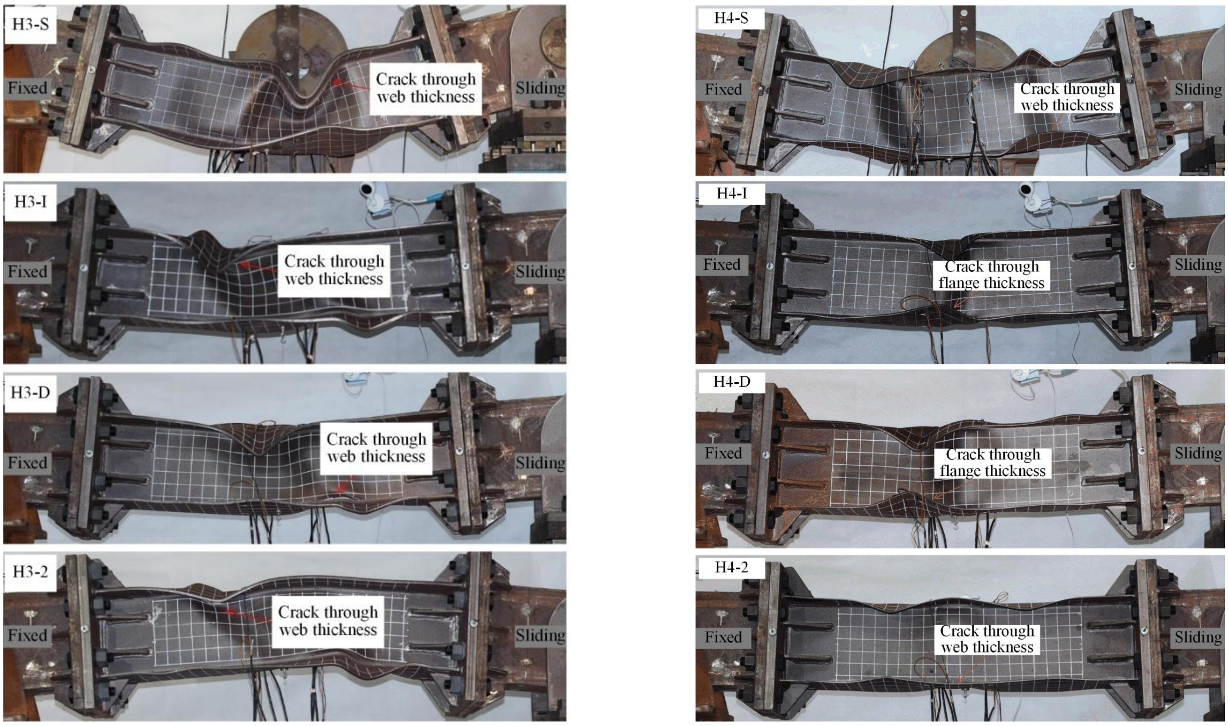

(a) Class 3 (b) Class 4

Fig. 6 Final states of specimens

3. Experimental results

3.1 Failure modes

All the specimens were cyclically tested to large plastic deformation. Commonly local buckling at the beam flanges first occurred, and cracks could initiate at either the beam flanges or the weld toes of the beam-web-to-beam-flange joints. The whole failure processes of Class 3 and 4 specimens are respectively given in Figs. 5(a) and (b), and the final states of the specimens are shown in Figs. 6(a) and (b), where cracks have run through either the beam webs or the flanges. It can be seen from Figs. 5(a) and 6(a) that the failure processes of the Class 3 specimens can be divided into the following stages:

- The beam flange edge yielded at a rotational angle of approximate 0.01 rad, and plastic deformation went on developing into the beam web;
- Local elasto-plastic buckling at the compressive beam flange occurred with small local deformation, and the buckling deformation developed as cyclic loading proceeded;
- The beam webs exceeded the elastic limit of the steel plates, and local buckling also occurred at the beam web due to decreased tangent modulus of the steel during the plastic state;
- Deformation concentrated at the local buckling locations, especially at the beam flanges and the weld toes of the beam-web-to-beam-flange joints, leading to crack initiation at either the beam flanges or the weld toes;
- All the cracks finally ran through the beam web thickness. This is mainly due to the non-smooth transition at the welds of the beam webs and the flanges and relatively low ductility at the boundary between te heat affected zone and the weld metal (Liu *et al*. 2017).

The failure processes of Class 4 specimens shown in Figs. 5(b) and 6(b) are different from those of Class 3 specimens, where the main differences lie in the following aspects:

- The beam flange of Class 4 specimens failed due to elastic local buckling but not elasto-plastic buckling;
- Local buckling deformation mainly concentrated at the beam flanges, while the deformation at the beam webs was relatively small compared with that of Class 3 specimens;
- Though crack initiation locations were similar to those of Class 3 specimens, crack propagated at both the beam flanges and the weld toes of the beam-web-to-beam-flange joints for Class 4 specimens.

The crack initiation locations and the rupture locations of the specimens are shown in Table 3, indicating most of the cracks initiated from the weld toes of the beam-web-to-beam-flange joints. The rupture locations of Class 4 specimens where the cracks first ran through the steel plate thickness are different from those of Class 3 ones. This implies that though the beam flanges have a slender cross section, the dominant factor affecting cracking of the specimens is still the relative poor ductile fracture resistances of the weld toes at the beam-web-to-beam-flange joints. The experimental results of Class 1 specimens with relatively compact beam flanges are different from those of Class 3 and Class 4 ones, where all the cracks initiated at the weld toes for Class 1 specimens. One reason for this difference is for the slender beam flanges of Class 3 and Class 4 specimens and corresponding relatively significant strain concentration at the beam flanges compared with Class 1 specimens. Another possible reason is for the decreasing fracture toughness of the flange material induced by the welding process. In this study, each specimen is welded using three plates. Since the thickness of the web plates are the same for all the specimens, and the welding heat input for all the specimens is also similar to each other. The thin-walled flanges of Class 3 and Class 4 specimens are more apt to be affected by the welding process, leading to a decreasing fracture toughness of the flange plates. This indicates that the cracks of the specimens with slender beam flanges tend to shift from the weld toes to the beam flanges due to the aforementioned reasons.

It is interesting to note that cracks all initiated from the weld toes of the beam-web-to-beam-flange joints for the specimens under the single full cycle loading and the 2-stage incremental loading. The final rupture of the four specimens, i.e., H3-S, H3-2, H4-S and H4-2, also all occurred at the weld toes. The main characteristic of the single full cycle loading is its extremely large rotation amplitude. No crack initiation occurred at the first half loop of Specimens H3-S and H4-S, but cracks soon occurred at the subsequent reversal loading. This indicates that the large strain amplitude makes cracks more apt to occur at the weld toes. This also implies that the material close to the weld toes under the extremely large strain amplitude has a relatively poor ULCF life compared with the one at the base metal of the flange.

The main characteristic of the 2-stage incremental loading compared with the incremental loading lies in its first stage loadings with a number of relatively small plastic loading reversals. This difference also leads to different cracking locations between the specimens under the 2-stage incremental loading and the incremental loading. This implies that the relatively small strain plastic loading reversals can shift the cracks from the base metal of the flange to the welds. In other words, the material close to the weld toes also has a relatively poor ULCF life at the small plastic strain range compared with that of the base metal in this study.

Fig. 7 shows the moment-rotation curves of Class 3 specimens with the critical moments of the specimens marked in the curves. It can be found that the peak loads are all beyond the elastic limit and close to the full-plastic moment of the cross section, indicating that the local buckling is elasto-plastic buckling. The failure process of Specimen H3-S can be divided into the following stages:

- The cross-sectional edge yielded, and the corresponding load is denoted as M_y as shown in Fig. 7;
- Significant decrease of the tangent stiffness of the load-displacement curve shown in Fig. 7(a) can be observed. Then local buckling at the compressive flange occurred when the rotation reached -0.04 rad, when the moment applied was below the cross-sectional full-plastic moment;
- The load continued increasing slightly till the peak load when the rotation reached -0.04 rad owing to strain hardening of the material, and the load-carrying capacity decreased subsequently due to excessive local buckling deformation at the compressive flange;
- A crack initiated at the weld toe of the compressive web-to-flange joint as shown in Fig. 5 when the rotation reached -0.24 rad. The crack propagated along the weld length direction, while the crack width was almost unchanged;
- The loading direction was reversed and the crack propagated quickly along both the weld length and the web thickness directions from the weld toe. The crack finally ran through the web thickness when the rotation reached 0.22 rad;
- Loss of the load-carrying capacity at the reversal loading half cycle due to excessive local buckling deformation and cracking.

Likewise, the failure process of Specimen H3-I can be divided into the following stages:

- The cross-sectional edge stress reached the yield strength of the material firstly;
- Local buckling occurred at the first loading cycle of the 0.03 rad amplitude as shown in Fig. 7(b) and the load increased a bit after the local buckling;
- The load-carrying capacity decreased due to excessive local buckling deformation at a rotation of 0.024 rad within the first loading cycle of the 0.04 rad amplitude;
- Minor cracks initiated at the top flange surface during the first loading cycle of the 0.06 rad amplitude;
- A crack at the weld toe of the top web-to-flange joint ran through the web thickness at the first loading cycle of the 0.07 rad amplitude.

For Specimen H3-D under the de-incremental loading history, the failure process can be divided into the following process:

- The cross-sectional edge stress reached the yield strength of the material firstly;
- Local buckling occurred at a rotation of -0.033 rad within the first loading cycle of the 0.05 rad amplitude during the decremental loading stage as shown in Fig. 7(c);
- The load-carrying capacity continued increasing slightly until the rotation reached -0.045 rad, and it then began to decrease as the local buckling deformation became apparent;
- A crack initiated at the bottom flange during the incremental loading stage at the first cycle of the 0.05 rad amplitude, where the load-carrying capacity is 84% of the peak load;
- As the loading amplitude increased, another crack at the weld toe of the bottom web-to-flange joint finally ran through the web thickness at the first cycle of the 0.07 rad amplitude.

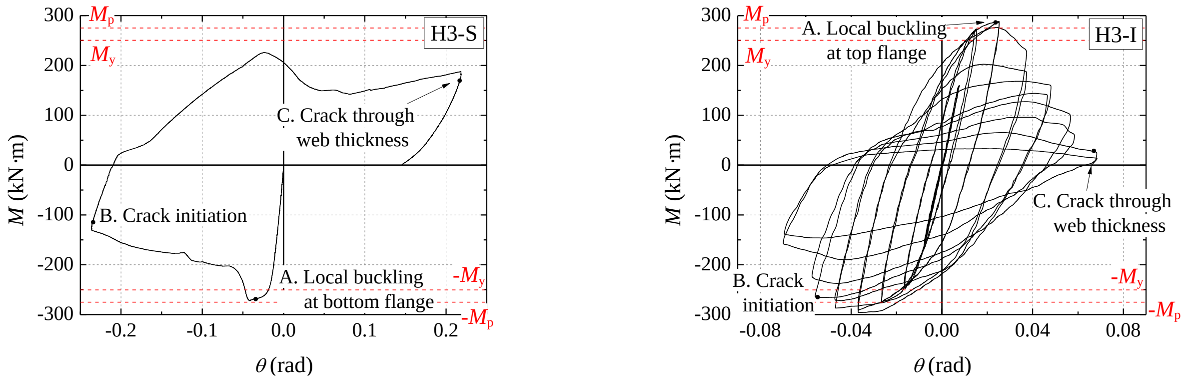

(a) Single full cycle loading

(b) Incremental loading

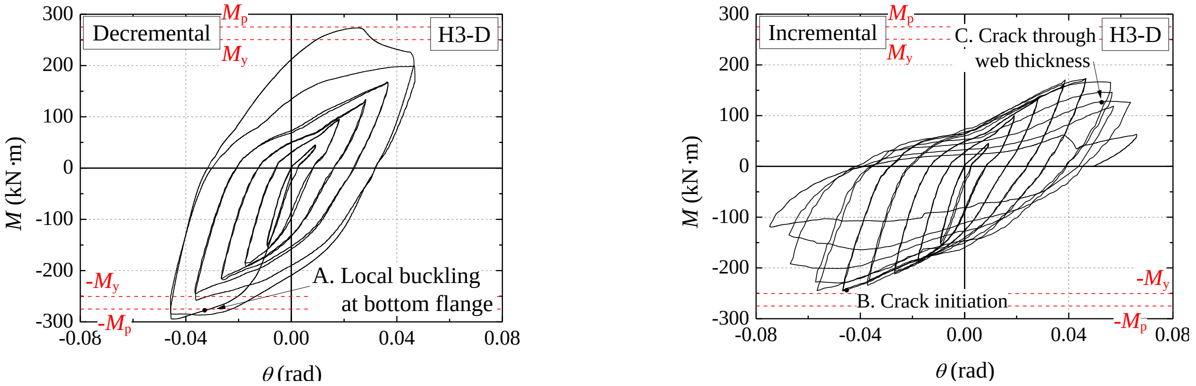

Decremental part

Incremental part

(c) De-incremental loading

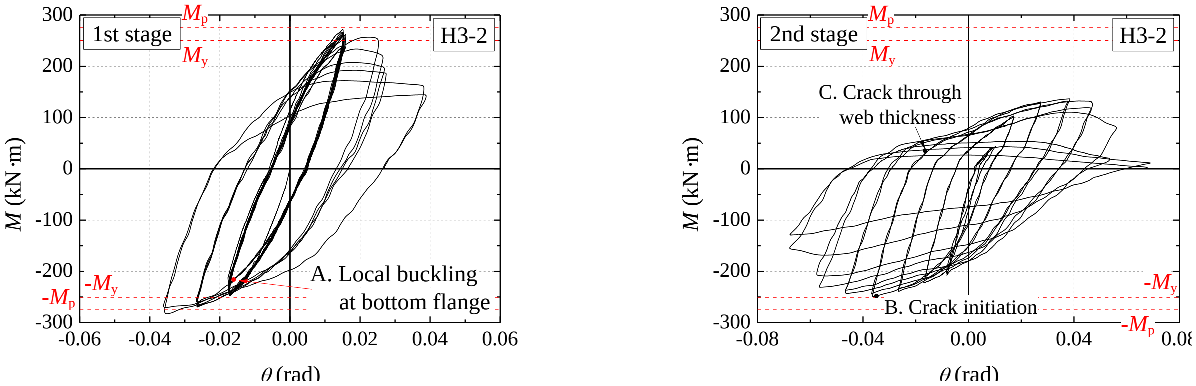

First stage

Second stage

(d) 2-stage incremental loading history

Fig. 7 Moment-rotation curves of Class 3 specimens

For Specimen H3-2, 12, 4 and 2 loading cycles were firstly applied for the amplitudes of 0.02 rad, 0.03 rad and 0.04 rad, respectively. Then an incremental loading history similar to that of Specimen H3-I was applied. The failure process is given as follows:

- The cross-sectional edge stress reached the yield strength of the material firstly;
- Local buckling occurred at the twelfth loading cycle of the 0.02 rad amplitude during the constant-amplitude loading stage, and no obvious decrease in the load was observed;
- Deterioration of the load-carrying capacity happened from the second loading cycle of the 0.03 rad amplitude during the constant-amplitude loading stage, and the load continued decreasing as the number of the loading cycles increased;
- Multiple minor cracks initiated at the top weld toe of the web-to-flange joint at the first loading cycle of the 0.04 rad amplitude during the incremental amplitude loading stage, and a main crack ran through the web thickness at the first loading cycle of the 0.07 rad amplitude.

The moments of local buckling, crack initiation and final rupture of the specimens are given in Table 3.

Comparison between the test results of Specimens H3-I and H3-2 shows that occurrence of local buckling is correlated with the loading histories, and preceding plastic reversals can lead to premature local buckling of the beam under a smaller rotation. Decrease of the load-carrying capacity is mainly induced by development of the local buckling deformation, especially for Class 4 specimens with slender cross sections. In addition, the specimens can still maintain a substantial load-carrying capacity at the moments of crack initiation, ranging from 0.90 to 1.06 times of the yielding moment for Class 3 specimens, and 0.42 to 0.82 for Class 4 specimens. This indicates that cracking is a secondary factor leading to deterioration of the load-carrying capacity.

The load-displacement curves of Class 4 specimens are shown in Fig. 8, indicating that the peak loads are all below the yield moment of the specimens. This implies that the local buckling is elastic buckling owing to the large width-to-thickness ratio.

The failure process of Specimen H4-S can be divided into the following stages:

- Local buckling at the compressive flange was induced before the cross-sectional edge reached the yield strength of the material, and the corresponding load is denoted as M_y as shown in Fig. 8;
- The load continued increasing till the peak load

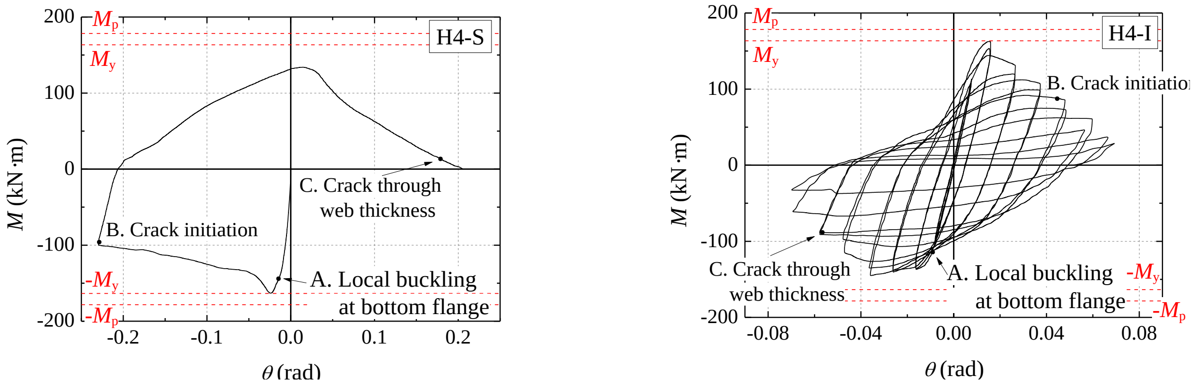

(a) Single full cycle loading

(b) Incremental loading

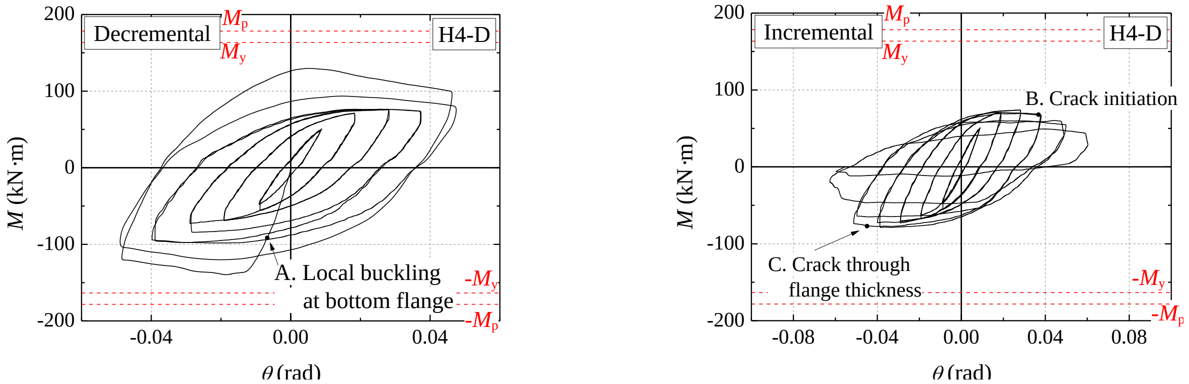

Decremental part

Incremental part

(c) De-incremental loading

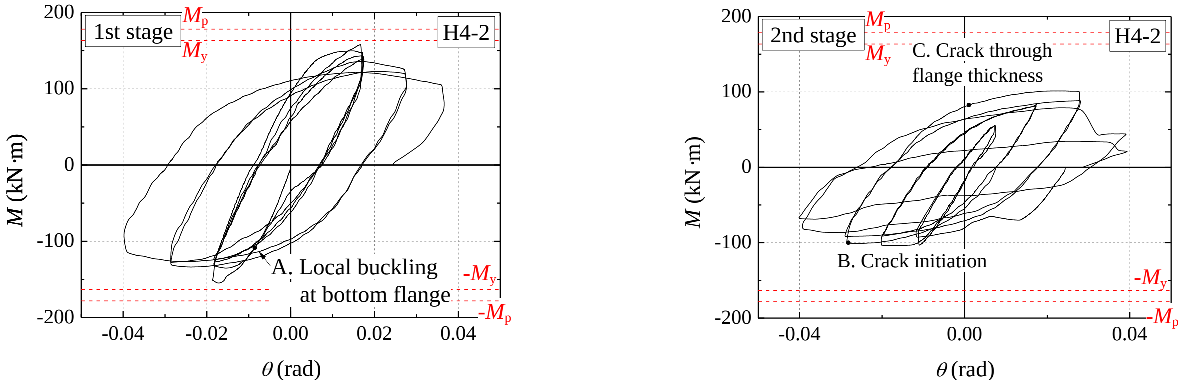

First stage

Second stage

(d) 2-stage incremental loading history

Fig. 8 Moment-rotation curves of Class 4 specimens

when the rotation reached -0.023 rad and the load-carrying capacity decreased due to excessive local buckling at the compressive flange;
- The loading direction was reversed and a crack initiated at the weld toe of the compressive web-to-flange joint when the rotation reached -0.23 rad;
- The crack propagated quickly along both the weld length and the web thickness directions from the weld toe. The crack finally ran through the web thickness when the rotation reached 0.18 rad.

Likewise, the failure process of Specimen H4-I can be divided into the following stages:

- Local buckling at the compressive flange was induced before the cross-sectional edge reached the yield strength of the material;
- The load at the compression side continued increasing till the peak load when the rotation reached -0.038 rad as shown in Fig. 8(b), and the load-carrying capacity decreased due to development of the local buckling deformation;
- Minor cracks initiated at the bottom flange surface at the first loading cycle of the 0.05 rad amplitude;
- The crack at the top flange ran through the flange thickness at the second loading cycle of the 0.06 rad amplitude.

Comparison between the test results of Specimens H4-S and H4-I implies that local buckling affected load-carrying capacity remarkably.

For Specimen H4-D under the de-incremental loading history, the failure process can be divided into the following stages:

- Local buckling at the compressive flange occurred before the cross-sectional edge reached the yield strength of the material;
- The load continued increasing till the peak load when the rotation reached -0.019 rad as shown in Fig. 8(c), and the load-carrying capacity decreased due to development of the local buckling deformation;
- A crack initiated at the weld toe of the bottom beam-web-to-beam-flange joint during the incremental loading stage at the first cycle of the 0.04 rad amplitude;
- Another crack at the bottom flange ran through the flange during the incremental loading stage at first cycle of the 0.05 rad amplitude.

For Specimen H4-2, 4, 2 and 1 loading cycles were firstly applied for the amplitudes of 0.02 rad, 0.03 rad and 0.04 rad, respectively. Then an incremental loading history similar to that of Specimen H4-I was applied. The failure process is given as follows:

- Local buckling at the compressive flange was induced before the cross-sectional edge reached the yield strength of the material;
- The load continued increasing till the peak load when the rotation reached -0.017 rad as shown in Fig. 8(d);
- The load-carrying capacity decreased to 65.4% of the peak load after the first stage loading with three constant amplitudes;
- Multiple minor cracks initiated at the top weld toe of the flange-to-web joint at the first loading cycle of the 0.03 rad amplitude during the second loading stage, and the crack ran through the web thickness at the reversal loading half cycle.

3.2 Hysteretic curves

The hysteretic curves of Class 3 and Class 4 specimens are respectively shown in Figs. 7 and 8, where the shuttle-shaped curves indicate stable hysteretic properties of the specimens. The pinching effect can be observed due to local buckling of the slender beam flanges. The specimens with Class 4 beam flanges and Class 1 beam webs can still dissipate a certain amount of energy owing to the compact beam webs, indicating that the seismic performance of the beam is not solely determined by the beam flange. In addition, the ratios of the load-carrying capacities at the moments of buckling and crack initiation to the corresponding cross-sectional edge yielding moment, M_y, are given in Table 3. The remained load-carrying capacity when buckling occurred ranged from 0.62 to 1.18 times the corresponding M_y, and that when crack initiated ranged from 0.42 to 1.06. This implies that the specimens still can maintain substantial load-carrying capacities after occurrence of the local buckling and cracking.

The skeleton curves of the hysteretic curves are shown in Fig. 9, which indicates that cyclic large plastic straining can lead to premature local buckling and also deterioration of the load-carrying capacity. In addition, the initial stiffness and the peak loads of the specimens are close to each other as shown in Fig. 9.

3.3 Ultra-low cycle fatigue life evaluation

Two ductility indices of a specimen are commonly employed, i.e., the maximum ductility, $\mu_{\max}$, and the cumulative plastic ratio, μ_c, which can be respectively given as follows

$$\mu_{max} = \frac{\theta_{max}}{\theta_y} \tag{2}$$

$$\mu_c = \sum \mu_{pi} = \sum \frac{\left|\theta_{pi}\right|}{\theta_y} = \sum \frac{\left|\theta_i\right| - \left|\frac{M_i}{K}\right|}{\theta_y} \tag{3}$$

where $\theta_{\max}$ = the maximum rotation corresponding to 85% of the peak load; θ_y = rotation corresponding to yielding of the cross-sectional edge; μ_{pi} = plastic ratio of the i-th loading half cycle; $|\theta_i|$ = absolute value of the rotation of the i-th loading half cycle as illustrated in Fig. 10; $|\theta_{pi}|$ = absolute value of the plastic rotation of the i-th loading half cycle as shown in the figure; M_i = maximum moment of the i-th loading half cycle; K = initial stiffness of the specimen. The values of $\mu_{\max}$ and μ_c are listed in Table 3, indicating

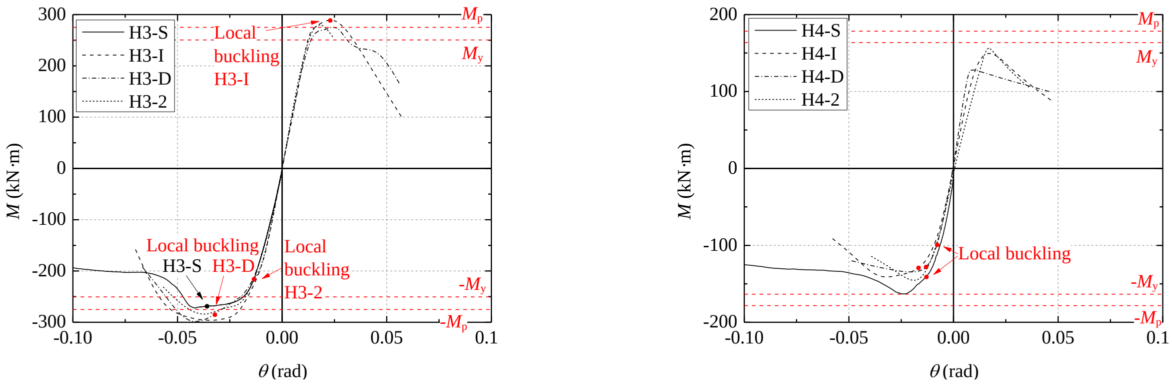

(a) Class 3 specimens (b) Class 4 specimens

Fig. 9 Skeleton curves of moment-rotation curves

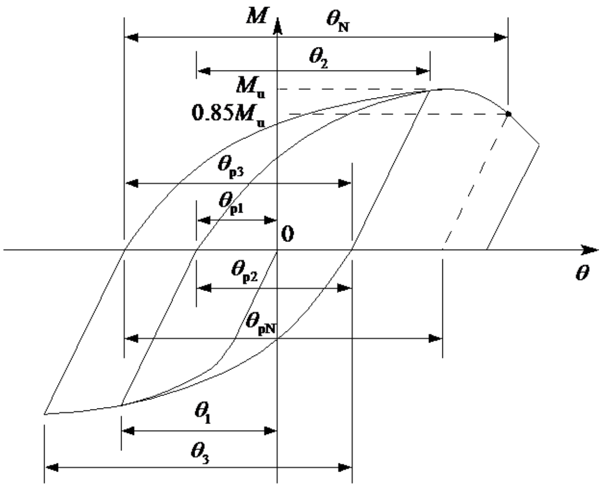

Fig. 10 Illustration of ductility index calculation (Zhao *et al.* 2018)

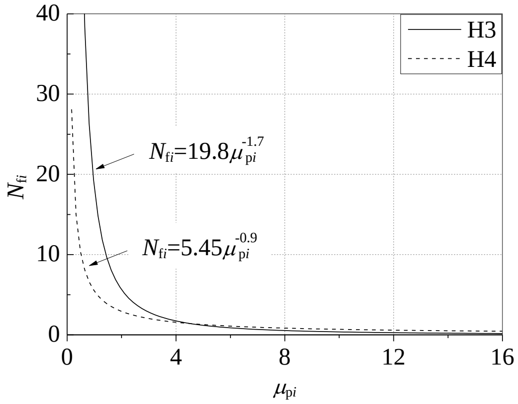

Fig. 11 Failure life prediction

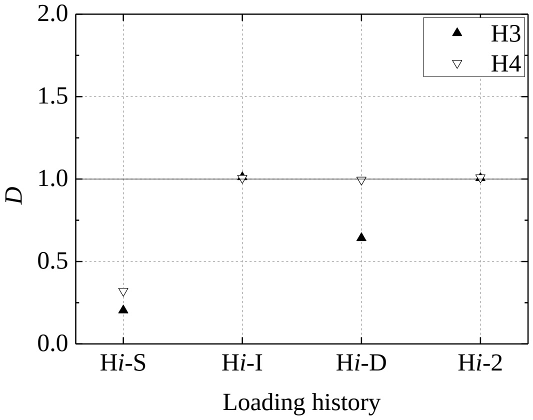

Fig. 12 Damage evaluation result using Eq. (6)

a remarkable effect of the loading history on the experimental results. Compared with the single full cycle loading history, the specimens under the other three loading histories had much larger ductility indices. In addition, the ductility indices decreased significantly with an increasing width-to-thickness ratio of the beam flange. Fig. 10 shows that failure is defined when the load decreases to 85% of the peak load, M_u.

To evaluate the ULCF lives of the specimens, the Manson-Coffin rule and the Miner's rule were employed simultaneously in this study. According to the Manson-Coffin rule, one can obtain the following equation

$$N_{fi} = C\mu_{pi}^{k} \tag{4}$$

where N_{fi} = number of loading half cycles under the constant-amplitude loading history with a plastic ratio of μ_{pi}; C, k = constants of the ULCF model.

An incremental damage index was defined according to the Miner's rule as

$$\Delta D_i = \frac{1}{N_{fi}} \tag{5}$$

where ΔD_i is the incremental damage during the *i*-th loading half cycle.

$$D = \sum_{i=1}^{N} \Delta D_i = \sum_{i=1}^{N} \frac{1}{C\mu_{pi}^{k}} \tag{6}$$

It is postulated that the ULCF life is expected when D reaches 1.0. The two constants C and k can be calibrated by comparison between the theoretical and the experimental results. The fitted C and k are respectively equal to 19.8 and

-1.7 for Class 3 specimens, and 5.45 and -0.9 for Class 4 specimens, indicating dependency of the values on the cross section. The equations for the ULCF life prediction of the Class 3 and Class 4 specimens are plotted in Fig. 11, and the predicted results are also compared with the experimental ones in Fig. 12, indicating that the equation can well evaluate the ULCF lives of all the specimens except for the single full cycle loading cases which are equivalent to those under monotonic bending. For the single full cycle loading cases, i.e., Specimens H3-S and H4-S, the main difference from the other six specimens is their large loading amplitudes, leading to an apparent overestimation of the ULCF life prediction according to Eq. (6).

4. Numerical simulation

4.1 Numerical modeling

Numerical simulations were conducted using the commercial finite element (FE) software ABAQUS to simulate the experimental results and investigate the capacity of the numerical simulation focused on the correlation between the stress states and local buckling of Class 3 and Class 4 specimens. Three-dimensional FE models using the four-node shell elements with reduced integration scheme, *S4R*, were established as shown in Fig. 13. The four pin connections of the loading beams were simulated using four reference nodes, where the freedoms of the nodes at the edges of pins were coupled with the corresponding reference nodes. The boundary constraints and enforced displacements were then directly applied to the corresponding reference nodes.

Initial geometric imperfection was considered by implementing the buckled configurations before conducting the elasto-plastic numerical simulations. The first three buckling modes were implemented according to Eq. (7), and the imperfection distribution Δx can be expressed as

$$\Delta x = \sum_{1}^{3} w_i \cdot \phi_i \tag{7}$$

where w_i = coefficient of the i-th buckling mode; and w_1 = 1%t_f, w_2 = 0.5% t_f, w_3 = 0.1% t_f (t_f is thickness of the beam flange); ϕ_i = configuration of the i-th buckling mode.

4.2 Plasticity model

The Chaboche model with a combined hardening rule in ABAQUS was utilized in the FE analyses. The kinematic hardening rule is described by the following formulae

$$\boldsymbol{\alpha} = \sum_{i}^{n} \boldsymbol{\alpha}_i \, ; \qquad d\boldsymbol{\alpha}_i = \frac{2}{3} C_i d\boldsymbol{\varepsilon}_{\mathrm{p}} - \gamma_i \cdot \boldsymbol{\alpha}_i \cdot d\varepsilon_{eq} \tag{8}$$

where α = total backstress; n = number of backstresses; α_i = i-th backstress; C_i and γ_i = material constants of the i-th backstress; dε_{p} = plastic strain increment; dε_{eq} = equivalent plastic strain increment. Integration of Eq. (8) under uniaxial stress state gives

$$\boldsymbol{\alpha} = \begin{cases} C_i / \gamma_i \cdot (1\text{-}\mathbf{e}^{-\gamma\varepsilon_{eq}}) & \text{when } \gamma_i \neq 0 \\ C_i \cdot \varepsilon_{eq} & \text{when } \gamma_i = 0 \end{cases} \tag{9}$$

In this study, three backstresses were employed with a backstress of linear formation and the other two of nonlinear formations. Based on comparison between the experimental and numerical results, the plasticity model parameters were determined as listed in Table 4.

4.3 Numerical results

The predicted buckling modes of the specimens are compared with those of the experiments in Fig. 14, and the buckling modes are generally similar to each other. The yield strength of the material at the flange of Class 3 is 448 MPa, and that of Class 4 and the web of Class 3 is 428 MPa. It can be found that both of the beam flanges yielded for Class 3 specimens, and parts of the beam web near the flanges also yielded. This implies that the local buckling is elasto-plastic buckling. For Class 4 specimens, only part of the flanges close to the buckled region yielded, while the beam web was elastic, indicating an elastic buckling of Class 4 specimens.

4.4 Comparison with experimental results

The predicted hysteretic curves of Class 3 and Class 4 specimens are respectively compared with the experimental ones in Figs. 15 and 16, and the peak loads generally compare well with each other. The comparison results of the

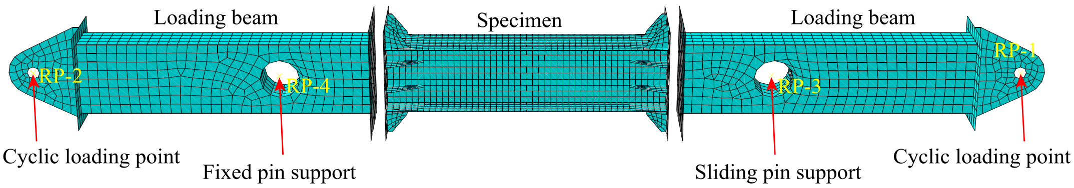

Fig. 13 FE model and mesh

Table 4 Plasticity model parameters

Location	Yield strength (MPa)	C_1	γ_1	C_2	γ_2	C_3	γ_3
Flange of H3	448	1852	19.3	704	19.3	721	0
Flange of H4 and web	428	2735	17.7	251	17.6	721	0

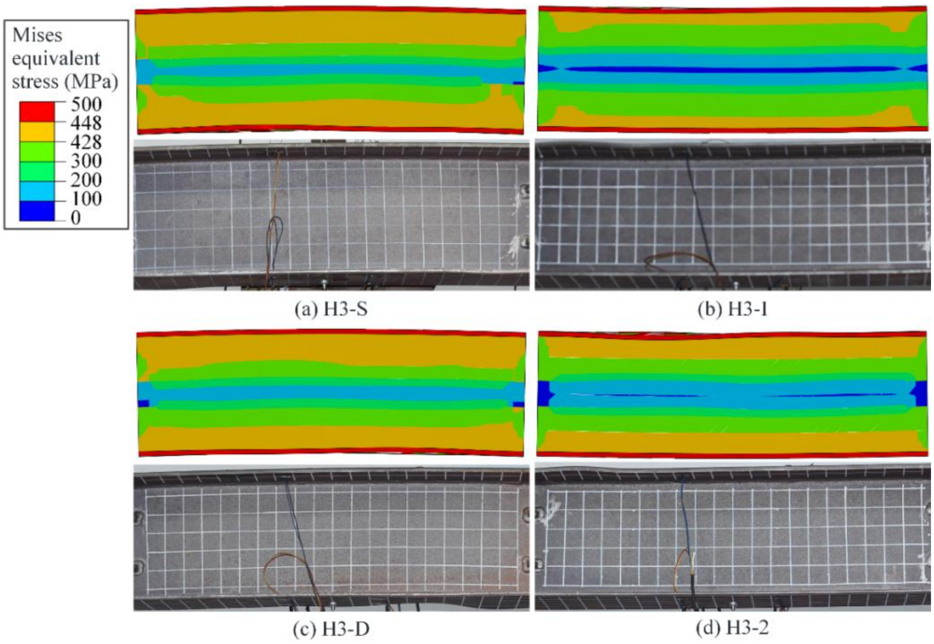

(a) Class 3

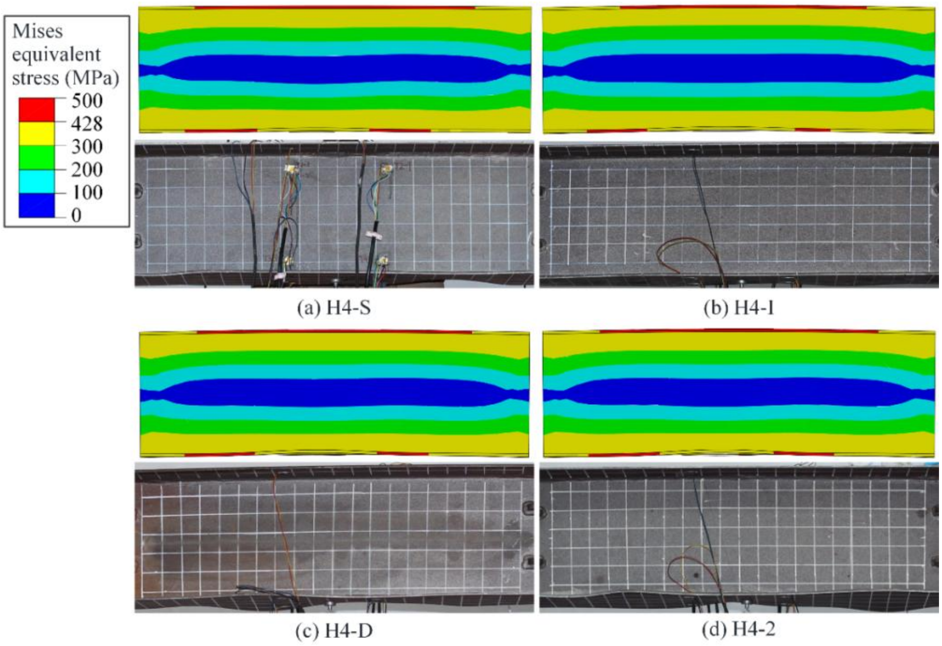

(b) Class 4

Fig. 14 Comparison of local buckling modes between experimental and numerical results

detailed values are also listed in Table 5. The comparison results indicate that the buckling loads of Class 3 specimens can be evaluated with acceptable accuracy, while those of Class 4 ones with large deviations. From the table, it can be found that the large deviations are mainly due to the poor prediction accuracy of the buckling instants under the cyclic loading. The comparison result of the single full cycle loading is better than those of the other ones. For example, buckling occurred at a rotation of 0.01 rad in the experiment, while at a rotation of 0.04 rad in the numerical simulation. The numerical results overestimate the loads at the transitions from elastic to plastic states, which may be due to the formation of the plasticity model, where the stresses at the transition regions are commonly overestimated. This can lead to overestimation of the buckling load. In addition, the instants when the local buckling occurred in the experiments and the simulations were also marked in the curves, and the comparison results show that the predicted instants of local buckling occurrence is earlier than those of the experimental ones. In future, ductile fracture models (Jia and Kuwamura 2015, Xiang *et al*. 2017, Vasdravellis *et al*. 2014) can be employed to further investigate the whole cracking behaviors of the specimens.

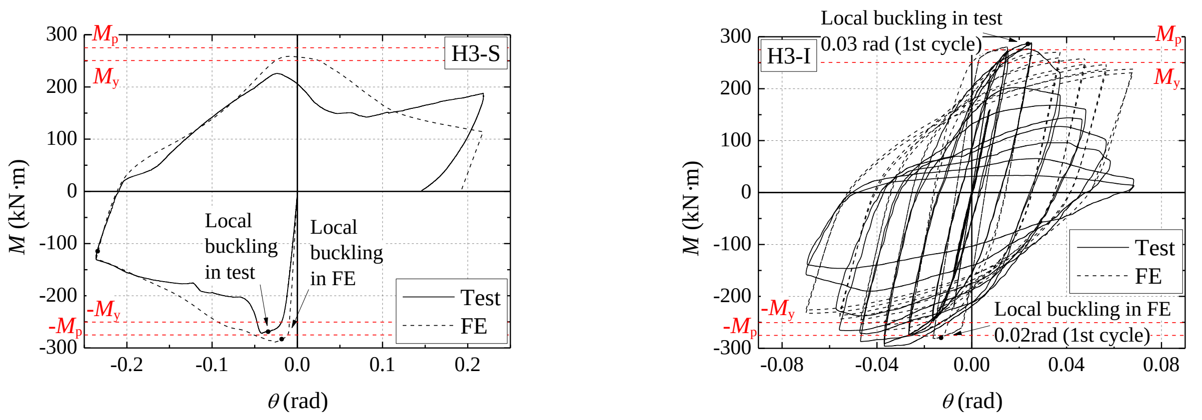

(a) H3-S (b) H3-I

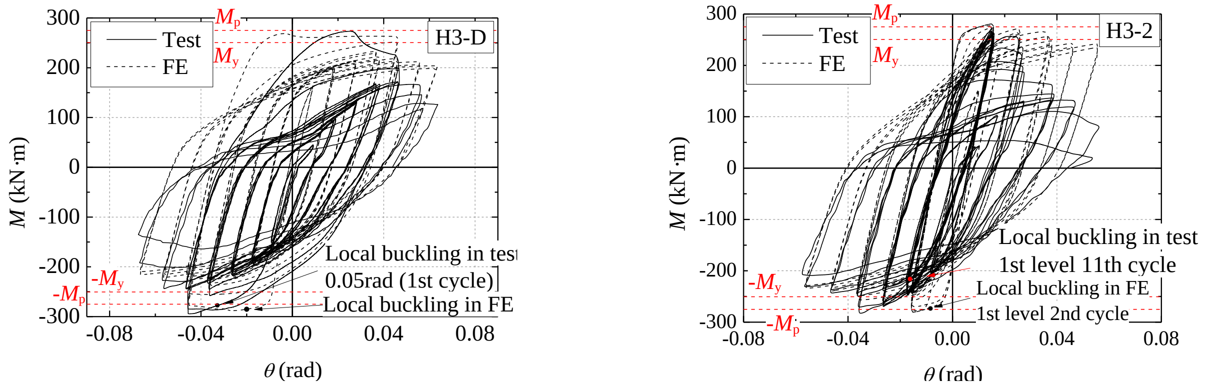

(c) H3-D (d) H3-2

Fig. 15 Comparison of H3 hysteretic curves between experimental and numerical results

Table 5 Comparison between experimental and numerical results

Specimens	$M_{u,FE}$ (kN.m)	$M_{u,FE}/M_{u,exp}$	$M_{b,FE}$ (kN.m)	$M_{b,FE}/M_{b,exp}$	Buckling of test	Buckling of FE
H3-S	289.1	1.07	283.7	1.13	0.04 rad	0.018rad
H3-I	282.4	0.95	278.0	1.13	0.03 rad (1st cycle)	0.02rad (1st cycle)
H3-D	282.5	0.96	285.3	1.14	0.04 rad (D-1st cycle)	0.02rad (D-1st cycle)
H3-2	282.5	1.00	271.6	1.34	0.02 rad (1st stage-12th cycle)	0.01rad (1st stage-2nd cycle)
H4-S	170.5	1.05	118.9	0.73	0.01 rad	0.007rad
H4-I	171.1	1.05	141.0	1.39	0.01 rad (2nd cycle)	0.007rad (1st cycle)
H4-D	171.0	1.22	95.7	0.59	0.01 rad (D-1st cycle)	0.005rad (D-1st cycle)
H4-2	170.0	1.08	69.6	0.43	0.01 rad (1st stage-1st cycle)	0.004rad (1st stage-1st cycle)

*Notes: $M_{u,FE}$ = ultimate moment of the numerical simulation; $M_{b,FE}$ = maximum moment capacity within the half cycle when buckling occurs in the numerical simulation. Buckling indicates when the buckling occurs

5. A proposed approach for cyclic flange local buckling problem

Based on a theory proposed in the literature (Kasai and Popov 1986a) for shear link beams, it was hypothesized that the solution to the elasto-plastic buckling problem could be obtained from the corresponding elastic buckling solution expressed as the following equation

$$\sigma_p = \eta(\sigma)\cdot\sigma_E \tag{10}$$

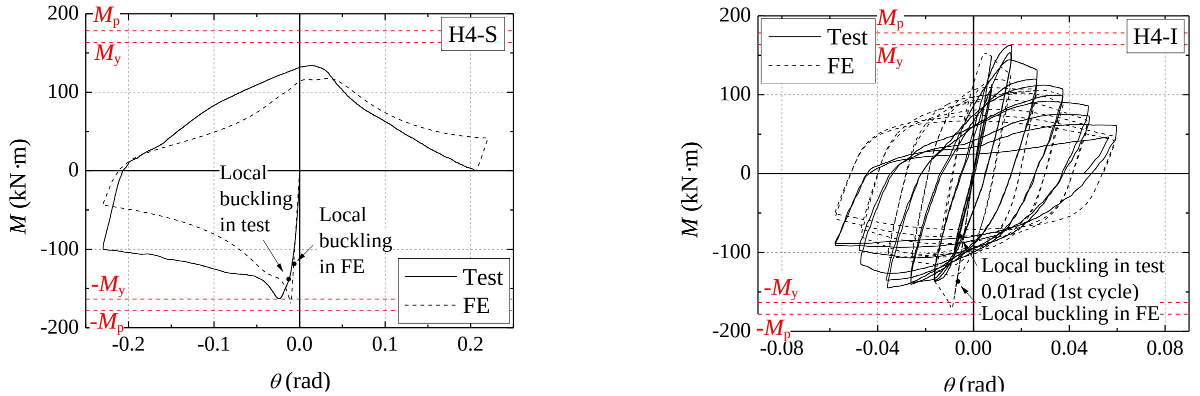

(a) H4-S (b) H4-I

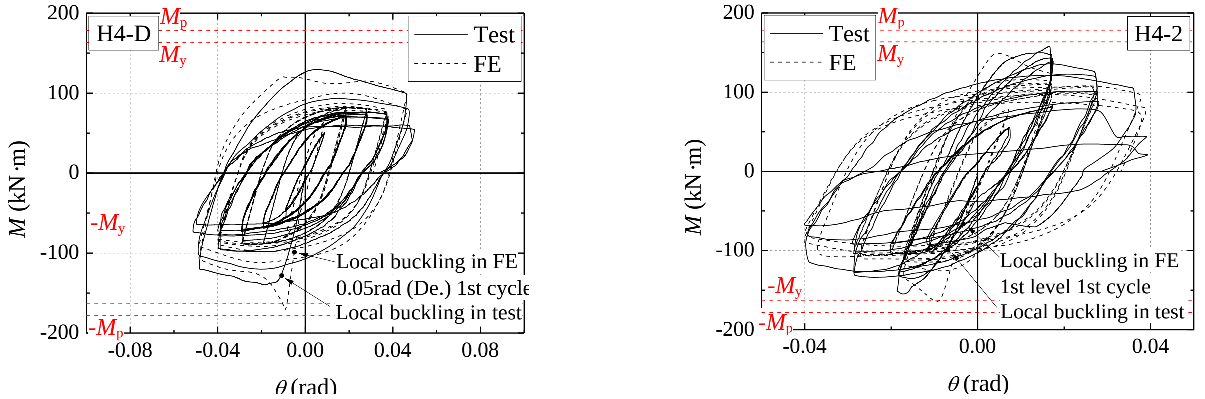

(c) H4-D (d) H4-2

Fig. 16 Comparison of H4 hysteretic curves between experimental and numerical results

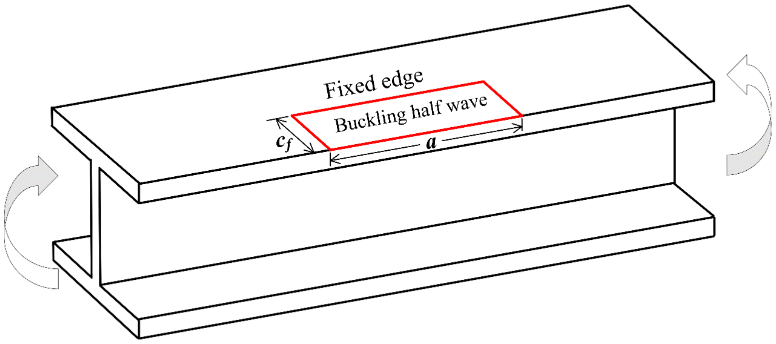

Fig. 17 Boundary conditions of a buckled plate at the compressive flange of a beam

in which η denotes a plastic-reduction factor, which is a function of the plastic strain-hardening history; and σ_E denotes the elastic buckling stress, which can be derived from the elastic buckling plate problem as Eq. (11)

$$\sigma_E = K_s \cdot \frac{\pi^2 E_0}{12(1-\nu^2)} \cdot \left(\frac{t}{c_f}\right)^2 \tag{11}$$

The compressive beam flange has a small length-to-width ratio, a / c_f, where a is the flange length at the compressive side, c_f is the cantilevered width of the flange. Three of its edges is fixed while the other one is free as shown in Fig. 17, the stability coefficient, K_s, can be approximately estimated as Eq. (12)

$$K_s = 0.425 + \left(\frac{a}{c_f}\right)^2 \approx 0.425 \tag{12}$$

where ν = Poisson's ratio, which is taken as 0.3 in this study.

In order to solve Eq. (10), the expression of η must be known. In this paper, an empirical approach to calculate the ratio of the plastic buckling stress to the elastic one at the maximum rotation angle, $\frac{\sigma_p}{\sigma_E}$, using experimental results was proposed. Although a complicated stress distribution can be expected to develop at the flange, it was simplified that the average flange stress σ_p at the maximum rotation angle has a linear relationship with M_u / W_{ey} and can be

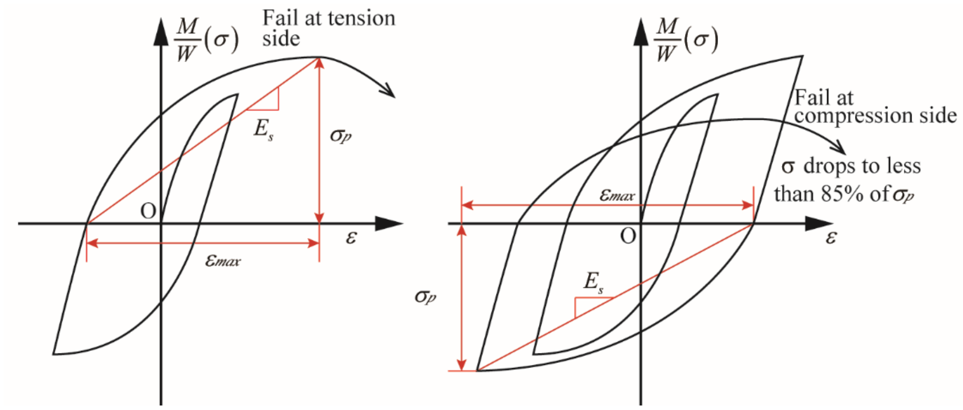

(a) Fail at the tension side (b) Fail at the compression side

Fig. 18 Definition of E_s and the maximum average flange strain and stress

expressed as Eq. (13)

$$\sigma_p = k_1 \cdot \frac{M_u}{W_{ey}} \tag{13}$$

in which k_1 = a plastic-reduction factor of the buckling stress; M_u = bending moment at the maximum rotation angle obtained from the experimental results; W_{ey} = the elastic section modulus of the tested beams. Then substituting Eq. (13) into Eq. (10) using the results obtained at the maximum rotation

$$\eta = \frac{\sigma_p}{\sigma_E} = k_1 \cdot \frac{M_u}{W_{ey}\sigma_E} \tag{14}$$

Based on an analogy to the shear link beams' results from the literature (Kasai and Popov 1986a), the secant modulus in bending beams' load-displacement curves illustrated in Fig. 18 can be defined as follows

$$E_s = \frac{\sigma_p}{\varepsilon} \tag{15}$$

where ε was measured from the farthest point of zero-bending moment reached during the entire previous history to the maximum rotation angle. From the mechanics of material, it is known that the cross-sectional curvature, ϕ, has a linear relationship with the strain as given in Eq. (16).

$$\phi = \frac{\varepsilon}{h/2} \tag{16}$$

where h is the distance of the material point to the neutral axis. In the pure bending problem, the cross-sectional curvature, ϕ, remains the same along the beam length, the rotation angle of the beam end at the maximum rotation, $\theta_{\max}$, is thus equal to integration of ϕ from one end to the mid-length of the beam at the maximum rotation state, as shown in Eq. (17)

$$\theta_{max} = \phi_{max} \cdot \frac{L}{2} = \frac{\varepsilon_{max}}{h/2} \cdot \frac{L}{2} = \frac{L}{h} \cdot \varepsilon_{max} \tag{17}$$

Now substituting Eqs. (13) and (17) into Eq. (15) with $\sigma = \sigma_p$ and $\varepsilon = \varepsilon_{\max}$, a relationship between E_s / E_0 and the test results M_u, $\theta_{\max}$ can be derived as Eq. (18)

$$\frac{E_s}{E_0} = k_1 \cdot \frac{L \cdot M_u}{h \cdot W_{ey}\theta_{max} \cdot E_0} \tag{18}$$

where E_0 is the Young's modulus, L is the beam length, h is the cross-sectional height. Then the values of η and E_s / E_0 for each specimen were calculated at the maximum rotation angle and plotted in Fig. 19.

Regardless of the loading history and the length-to-width ratio of the beam web, a good correlation between η and E_s / E_0 was obtained. The linear relation between η and E_s / E_0 was then calculated as Eq. (19)

$$\eta = 2.21 \frac{E_s}{E_0} \tag{19}$$

In order to obtain the relationship between the maximum rotation angle of the beam end, $\theta_{\max}$, and the length-to-width ratio of the flange, a / c_f. Equations (18) and (19) can be substituted into Eq. (10), with $\sigma = \sigma_p$ and $\varepsilon = \varepsilon_{\max}$ at the maximum rotation, leading to

$$\theta_{max} = 9.82 \cdot \frac{\sigma_E}{E_0} \tag{20}$$

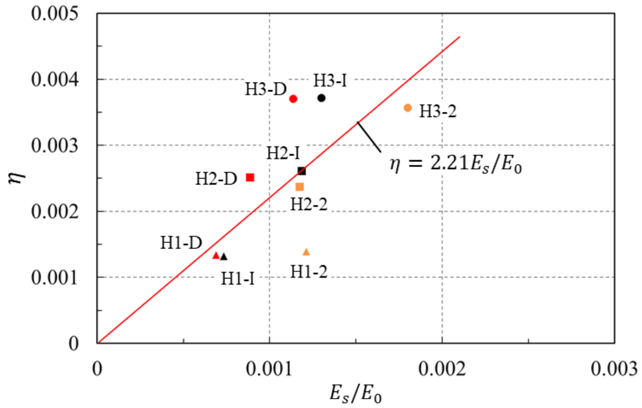

Fig. 19 Experimental relationships between η and E_s / E_0

According to Eq. (11), a simplified version of Eq. (20) can be obtained

$$\theta_{max} = 3.77\left(\frac{t}{c_f}\right)^2 \tag{21}$$

Eq. (21) is a simple relationship showing that $\theta_{\max}$ is a function of the width-to-thickness ratio of the beam flange, c_f / t. It can be used to predict cyclic rotational capacity of H-shaped steel beams under ultra-low-cycle pure bending. However, there is a prerequisite for the application of this equation that the beam web is Class 1 cross section.

6. Conclusions

In this study, an experimental study was conducted for Class 3 and Class 4 H-shaped steel beams under cyclic pure bending within the scope of ultra-low-cycle fatigue (ULCF). Effects of loading history and width-to-thickness ratio on failure modes, strength, cyclic rotational capacity and cumulative energy dissipation capacity were investigated. A theoretical analysis on the correlation of the cyclic rotational capacity and the width-to-thickness ratio was also conducted. Based on the experimental and theoretical results, the following conclusions can be drawn:

(1) Stable hysteretic curves were obtained for Class 3 and Class 4 H-shaped steel beams under ULCF loading, and a slight pinching effect was observed. It was found that the load-carrying capacity could continue increasing slightly even after occurrence of local buckling at the compressive flange owing to the strain hardening effect of the compact web plates, especially for the Class 4 specimens.

(2) Failure of Class 3 and 4 H-shaped steel beams under ULCF loading was mainly due to excessive development of the local buckling deformation at both the compressive flange and the web. The remained load-carrying capacity when buckling occurred ranged from 0.62 to 1.18 times the corresponding M_y, and that when crack initiated ranged from 0.42 to 1.06. The load-carrying capacity has decreased below 85% of the peak load when local buckling occurred. Local buckling and cracking are respectively the main and secondary reasons leading to strength deterioration of the Class 3 and Class 4 H-shaped steel beams.

(3) The proposed cumulative damage index based on the Manson-Coffin rule increases nonlinearly as the loading amplitude increases, which can compare well with the experimental results except for the cases under the single full cycle loading.

(4) Cracks can either initiate at the beam flange or the weld toe at the web-to-flange joint for Class 3 and Class 4 specimens, and the final rupture all occurred at the weld toe of web-to-flange joint for Class 3 specimens. For Class 4 specimens, the final rupture can either occurred at the beam flange or the weld toe. This indicates that cracking tends to shift from the weld toe to the beam flange as the width-to-thickness of the flange increases.

(5) For Class 3 specimens, numerical results indicate that the local buckling is elasto-plastic buckling, and part of the beam web also yielded when local buckling occurred. For Class 4 specimens, the local buckling is elastic buckling, where only the buckled region of the beam flange yielded when the local buckling occurred.

(6) The cyclic rotational capacity of H-shaped steel beams under ultra-low-cycle pure bending was found to be inversely proportional to the square of the width-to-thickness ratio of the beam flange, and a formula predicting the cyclic rotational capacity was proposed. The predicted results compared well with the experimental ones, which is applicable to H-shaped steel beams with Class 1 beam webs under ultra-low-cycle pure bending.

Acknowledgments

This study is supported by National Key R&D Program of China (2016YFC0701603) and National Natural Science Foundation of China (51178332, 51508401), which is greatly appreciated. This study is also partially supported by the Fundamental Research Funds for the Central Universities.

References

Akrami, V. and Erfani, S. (2015), "Effect of local web buckling on the cyclic behavior of reduced web beam sections (RWBS)", *Steel Compos. Struct., Int. J.*, **8**(3), 641-657.

Anastasiadis, A., Mosoarca, M. and Gioncu, V. (2012), "Prediction of available rotation capacity and ductility of wide-flange beams: Part 2: Applications", *J. Constr. Steel Res.*, **68**(1), 176-191.

CEN (2005), Eurocode 3: Design of steel structures Part 1-1: General rules and rules for buildings.

Chen, Y.Y., Pan, L.L. and Jia, L.-J. (2017), "Post-buckling ductile fracture analysis of panel zones in welded steel beam-to-column connections", *J. Constr. Steel Res.*, **132**, 117-129.

Cheng, X., Chen, Y. and Nethercot, D.A. (2013), "Experimental study on H-shaped steel beam-columns with large width-thickness ratios under cyclic bending about weak-axis", *Eng. Struct.*, 49, 264-274.

Coffin, L.A. (1954), "A study of the effects of cyclic thermal stresses on a ductile metal", *Trans. ASME*, **76**, 931-950.

Elkady, A. and Lignos, D.G. (2015), "Analytical investigation of the cyclic behavior and plastic hinge formation in deep wide-flange steel beam-columns", *B. Earthq. Eng.*, **13**(4), 1097-1118.

Erdal, F. (2015), "Effect of stiffeners on failure analyses of optimally designed perforated steel beams", *Steel Compos. Struct., Int. J.*, **22**(1), 183-201.

Ge, H.B., Jia, L.-J., Kang, L. and Suzuki, T. (2014), "Experimental study on seismic performance of partial penetration welded steel beam-column connections with different fillet radii", *Steel Compos. Struct., Int. J.*, **17**(6), 851-865.

Gioncu, V. and Petcu, D. (1997a), "Available rotation capacity of wide-flange beams and beam-columns Part 1. Theoretical approaches", *J. Constr. Steel Res.*, **43**(1-3), 161-217.

Gioncu, V. and Petcu, D. (1997b), "Available rotation capacity of wide-flange beams and beam-columns Part 2. Experimental and numerical tests", *J. Constr. Steel Res.*, **43**(1-3), 219-244.

Gioncu, V., Mosoarca, M. and Anastasiadis, A. (2012), "Prediction of available rotation capacity and ductility of wide-flange beams: Part 1: DUCTROT-M computer program", *J. Constr. Steel Res.*, **69**(1), 8-19.

Hasegawa, R. and Ikarashi, K. (2014), "Strength and plastic deformation capacity of H-shaped beam-columns", IABSE Symposium Report.

Jia, L.-J. and Kuwamura, H. (2015), "Ductile fracture model for structural steel under cyclic large strain loading", *J. Constr. Steel Res.*, **106**, 110-121.

Jia, L.-J., Koyama, T. and Kuwamura, H. (2014), "Experimental and numerical study of postbuckling ductile fracture of heat-treated SHS stub columns", *J. Struct. Eng.* (ASCE), **140**(7), 04014044.

Jia, L.-J., Ikai, T., Shinohara, K. and Ge, H.B. (2016), "Ductile crack initiation and propagation of structural steels under cyclic combined shear and normal stress loading", *Constr. Build. Mater.*, **112**, 69-83.

Jia, L.-J., Ge, H.B., Maruyama, R. and Shinohara, K. (2017), "Development of a novel high-performance all-steel fish-bone shaped buckling-restrained brace", *Eng. Struct.*, **138**, 105-119.

Jia, L.-J., Ge, H.B., Xiang, P. and Liu, Y. (2018a), "Seismic performance of fish-bone shaped buckling-restrained braces with controlled damage process", *Eng. Struct.*, **169**, 141-153.

Jia, L.-J., Li, R.-W., Xiang, P., Zhou, D.-Y. and Dong, Y. (2018b), "Resilient steel frames installed with self-centering dual-steel buckling-restrained brace", *J. Constr. Steel Res.*, **149**, 95-104.

Jia, L.-J., Dong, Y., Ge, H.B., Kondo, K. and Xiang, P. (2019), "Experimental study on high-performance buckling-restrained braces with perforated core plates", *Int. J. Struct. Stab. Dy.*, **19**(1), 1940004.

Kasai, K. and Popov, E.P. (1986a), "General behavior of WF steel shear link beams", *J. Struct. Eng.* (ASCE), **112**(2), 362-382.

Kasai, K. and Popov, E.P. (1986b), "Cyclic web buckling control for shear link beams", *J. Struct. Eng.* (ASCE), **112**(3), 505-523.

Krawinkler, H. (1992), Guidelines for cyclic seismic testing of components of steel structures, Applied Technology Council.

Kwon, Y.B., Kim, G.D. and Kwon, I.K. (2014), "Compression tests of cold-formed channel sections with perforations in the web", *Steel Compos. Struct., Int. J.*, **16**(6), 657-679.

Lee, G.C. and Lee, E.T. (1994), "Local buckling of steel sections under cyclic loading", *J. Constr. Steel Res.*, **29**(1-3), 55-70.

Liu, Y., Jia, L.-J., Ge, H.B., Kato, T. and Ikai, T. (2017), "Ductile-fatigue transition fracture mode of welded T-joints under quasi-static cyclic large plastic strain loading", *Eng. Fract. Mech.*, **176**, 38-60.

Manson, S.S. (1953), "Behavior of materials under conditions of thermal stress", *Proceedings of the Heat Transfer Symposium*, University of Michigan Engineering Research Institute, pp. 9-75.

Morkhade, S.G. and Gupta, L.M. (2017), "Experimental investigation for failure analysis of steel beams with web openings", *Steel Compos. Struct., Int. J.*, **23**(6), 647-656.

Nakashima, M. (1994), "Variation of ductility capacity of steel beam-columns", *J. Struct. Eng.* (ASCE), **120**(7), 1941-1960.

Newell, J.D. and Uang, C.M. (2008), "Cyclic behavior of steel wide-flange columns subjected to large drift", *J. Struct. Eng.* (ASCE), **134**(8), 1334-1342.

Richards, P.W. and Uang, C.M. (2005), "Effect of flange width-thickness ratio on eccentrically braced frames link cyclic rotation capacity", *J. Struct. Eng.* (ASCE), **131**(10), 1546-1552.

Vasdravellis, G., Karavasilis, T.L. and Uy, B. (2014), "Design rules, experimental evaluation, and fracture models for high-strength and stainless-steel hourglass shape energy dissipation devices", *J. Struct. Eng.* (ASCE), **140**(11), 04014087.

Xiang, P., Jia, L.-J., Ke, K., Chen, Y.Y. and Ge, H.B. (2017), "Ductile cracking simulation of uncracked high strength steel using an energy approach", *J. Constr. Steel Res.*, **138**, 117-130.

Zhao, X.Z., Tian, Y.F., Jia, L.-J. and Zhang, T. (2018), "Ultra-low cycle fatigue tests of Class 1 H-shaped steel beams under cyclic pure bending", *Steel Compos. Struct., Int. J.*, **26**(4), 439-452.

BU